RSC Advances

ROYAL SOCIETY OF CHEMISTRY

PAPER

View Article Online
View Journal | View Issue

Cite this: *RSC Adv.*, 2024, **14**, 13915

Aluminium phosphide ($Al_{12}P_{12}$) nanocage as a potential sensor for volatile organic compounds: A DFT study†

Mahmoud A. A. Ibrahim, *[ab] Manar H. A. Hamad, [a] Nayra A. M. Moussa, [a] Omar H. Abd-Elkader,[c] Shaban R. M. Sayed,[d] Muhammad Naeem Ahmed, [e] Ahmed M. Awad[f] and Tamer Shoeib *[g]

The efficacy of aluminium phosphide ($Al_{12}P_{12}$) nanocage toward sensing methanol (MeOH) and ethanol (EtOH) volatile organic compounds (VOCs) was herein thoroughly elucidated utilizing various density functional theory (DFT) computations. In this perspective, MeOH⋯ and EtOH⋯$Al_{12}P_{12}$ complexes were investigated within all plausible configurations. According to the energetic features, the EtOH⋯$Al_{12}P_{12}$ complexes exhibited larger negative values of adsorption and interaction energies with values up to −27.23 and −32.84 kcal mol^{-1}, respectively, in comparison to the MeOH⋯$Al_{12}P_{12}$ complexes. Based on the symmetry-adapted perturbation theory (SAPT) results, the electrostatic forces were pinpointed as the predominant component beyond the adsorption process within the preferable MeOH⋯ and EtOH⋯ $Al_{12}P_{12}$ complexes. The findings of the noncovalent interaction (NCI) index and quantum theory of atoms in molecules (QTAIM) outlined the closed-shell nature of the interactions within the studied complexes. Substantial variations were found in the molecular orbitals distribution patterns of MeOH/EtOH molecules and $Al_{12}P_{12}$ nanocage, outlining the occurrence of the adsorption process within the complexes under investigation. Thermodynamic parameters were denoted with negative values, demonstrating the spontaneous exothermic nature of the most favorable complexes. New energy states were observed within the extracted density of states plots, confirming the impact of adsorbing MeOH and EtOH molecules on the electronic properties of the $Al_{12}P_{12}$ nanocage. The appearance of additional peaks in Infrared Radiation (IR) and Raman spectra revealed the apparent effect of the adsorption process on the features of the utilized sensor. The emerging results declared the potential uses of $Al_{12}P_{12}$ nanocage as a promising candidate for sensing VOCs, particularly MeOH and EtOH.

Received 9th March 2024
Accepted 19th April 2024

DOI: 10.1039/d4ra01828a

rsc.li/rsc-advances

1. Introduction

In the contemporary world, scientists have focused significantly on developing sustainable nanomaterials for various applications, including energy, environment, and drug delivery. Indeed, the continued life of our planet depends significantly on advancements in sophisticated materials science. Several nano-based structures have been accordingly developed and were widely investigated, comprising fullerenes,[1] nanotubes,[2] and nanocones.[3]

More recently, the utilization of phosphide nanocages has attracted the attention of scientists.[4–6] It is worth mentioning that inorganic aluminium phosphide ($Al_{12}P_{12}$) nanocage was earlier distinguished by its distinctive chemical features, including a high energy gap and low electron attraction.[7–9] The potential applications of $Al_{12}P_{12}$ in non-linear optics,[10] drug carriers,[11,12] and sensors[13,14] have garnered tremendous attention. As an appropriate sensing material, the adsorption of cyanogen chloride and hydrogen cyanide toxic gases on the surface of $Al_{12}P_{12}$ was investigated.[15] Moreover, the sensitivity of the $Al_{12}P_{12}$ nanocarrier toward detecting phosgene gas was revealed.[16]

The increase in energy consumption and industrial activities made monitoring air pollution an essential priority for several

[a]*Computational Chemistry Laboratory, Chemistry Department, Faculty of Science, Minia University, Minia 61519, Egypt. E-mail: m.ibrahim@compchem.net*
[b]*School of Health Sciences, University of KwaZulu-Natal, Westville Campus, Durban 4000, South Africa*
[c]*Department of Physics and Astronomy, College of Science, King Saud University, P.O. Box 2455, Riyadh 11451, Saudi Arabia*
[d]*Department of Botany and Microbiology, College of Science, King Saud University, P.O. Box 2455, Riyadh 11451, Saudi Arabia*
[e]*Department of Chemistry, The University of Azad Jammu and Kashmir, Muzaffarabad 13100, Pakistan*
[f]*Department of Chemistry, California State University Channel Islands, Camarillo, California 93012, USA*
[g]*Department of Chemistry, The American University in Cairo, New Cairo 11835, Egypt. E-mail: t.shoeib@aucegypt.edu*

† Electronic supplementary information (ESI) available. See DOI: https://doi.org/10.1039/d4ra01828a

countries and organizations.[17–23] As a point of departure, volatile organic compounds (VOCs) are categorized as organic compounds with low water solubility, low boiling points, and high vapor pressure.[24,25] Detailedly, VOCs are considered hazardous air pollutants and are among the most frequent air pollutants released by industrial chemical processes, standard household products, and construction materials.[26–28] The natural environment and human health are significantly threatened by VOCs, which act as precursors to ozone and photochemical smog.[29–31] VOCs are the main contributor to the greenhouse effect and also have the possibility to damage the human nervous and circulatory systems.[32,33] Considering the risks of VOCs exposure, these compounds need to be eliminated from the environment. Several VOCs purification techniques have been developed, including adsorption,[34,35] biodegradation,[36] and membrane separation.[37] Numerous alcohols, including methanol (MeOH), ethanol (EtOH), isopropanol, ethylene glycol, *etc.*,[38] are commonly found as VOCs in various indoor air conditions. The adsorption amplitude of the $MoSe_2$ nanosheet and carbon nanopores toward adsorbing the MeOH and EtOH was earlier divulged.[39,40] Notwithstanding the promising properties of aluminium-bearing nanocages, no solid investigation revealed their efficiency in detecting the MeOH and EtOH molecules.

In this regard, the principal purpose of this study was to elucidate the potentiality of $Al_{12}P_{12}$ toward sensing the MeOH and EtOH molecules within all plausible configurations of the MeOH··· and EtOH···$Al_{12}P_{12}$ complexes. Geometrical optimization and frequency computations were executed for all the investigated systems, accompanied by adsorption and interaction energy calculations. To shed light on the physical forces dominating the adsorption process, the SAPT method was employed. Subsequently, the thermodynamic features, global indices of reactivity, and electronic parameters were assessed. This study will provide significant principles for the design and enhancement of $Al_{12}P_{12}$ nanocage applications in detecting toxic molecules, particularly for VOCs.

2. Results and discussion

2.1. ESP analysis

Molecular electrostatic potential (MEP) maps were portrayed for the optimized structures to clarify the electrophile and nucleophile sites, as recommended in literature.[41] Different colors were utilized to depict the difference in ESP at the molecular surface. In the colored scale, the red/orange/yellow, green, and blue colors-refer to electron-rich, neutral, and electron-deficient sites, respectively. A quantitative insight was subsequently provided by computing the surface electrostatic potential extrema values ($V_{s,min}/V_{s,max}$) over the surface of the optimized monomers. Fig. 1 illustrates the MEP maps and $V_{s,min}/V_{s,max}$ values.

As displayed in Fig. 1, the pure $Al_{12}P_{12}$ nanocage exhibits T_h symmetry and is composed of eight hexagonal rings in combination with six tetragonal rings.[42] At first glance, two different bonds in the $Al_{12}P_{12}$ nanocage were denoted. The first Al···P bond is shared by tetragonal and hexagonal rings with an

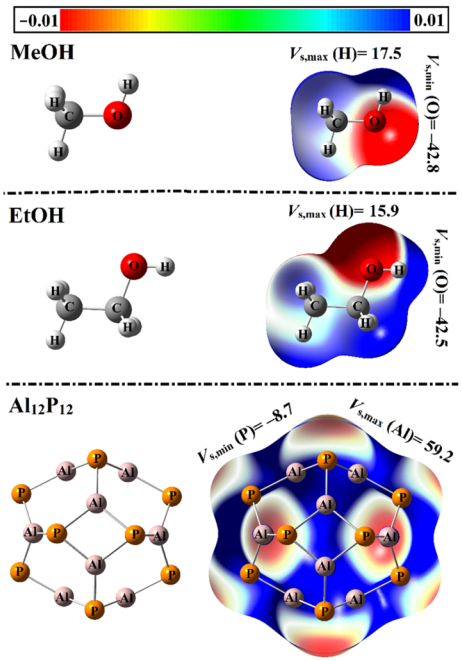

Fig. 1 Optimized structures of VOCs and $Al_{12}P_{12}$ nanocage combined with the MEP maps and $V_{s,min}/V_{s,max}$ values (in kcal mol^{-1}).

average bond length of 2.28 Å. Meanwhile, the other Al···P bond is located between two hexagonal rings with a bond distance of 2.33 Å. The MEP plots of the MeOH and EtOH clarified the nucleophilic site at the region enclosing the O atoms. Such pictorial outcomes were ensured by the existence of negative $V_{s,min}$ values of −42.8 and −42.5 kcal mol^{-1} over the surface of the MeOH and EtOH, respectively. At the same time, the electrophilic sites were observed *via* the existence of blue-colored regions around C and H atoms in the MeOH and EtOH molecules. On the surface of the $Al_{12}P_{12}$ nanocage, the red-colored nucleophilic and blue-colored electrophilic regions were around P and Al atoms with $V_{s,min}$ and $V_{s,max}$ values of −8.7 and 59.2 kcal mol^{-1}, respectively.

2.2. Adsorption features

To gain an extensive comprehension of the adsorption process, the VOCs were placed on the surface of the $Al_{12}P_{12}$ nanocage. Geometrical optimization calculations were executed for the VOC···$Al_{12}P_{12}$ complexes within all plausible configurations (Fig. 2). No imaginary frequency was identified, confirming that the optimized structures are true minima. On the optimized VOC···$Al_{12}P_{12}$ complexes, the MEP maps were extracted and are displayed in Fig. 2. The adsorption (E_{ads}) and interaction (E_{int}) energies were accordingly assessed. Table 1 shows the computed E_{ads} and E_{int} values along with the intermolecular distances between the VOC molecule and $Al_{12}P_{12}$ nanocage.

According to data presented in Table 1, the intermolecular distances were observed with values ranging from 4.45 to 1.97 and 3.30 to 1.95 Å for the optimized MeOH··· and EtOH··· $Al_{12}P_{12}$ complexes, respectively. Notably, the VOC···$Al_{12}P_{12}$ complexes exhibited significant negative E_{ads} and E_{int} values,

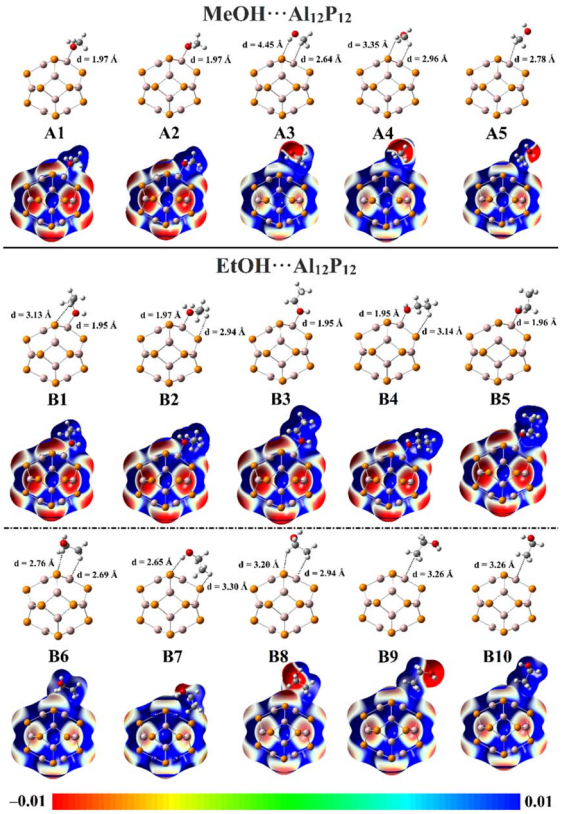

Fig. 2 Optimized structures and MEP maps of the MeOH··· and EtOH···$Al_{12}P_{12}$ complexes within all plausible configurations. The intermolecular distances are in Å.

Table 1 Calculated values of the adsorption energies (E_{ads}, kcal mol^{-1}) and the interaction energies (E_{int}, kcal mol^{-1}) of the optimized MeOH··· and EtOH···$Al_{12}P_{12}$ complexes within all plausible configurations in conjunction with intermolecular distances (d, Å)

Complexes	Configuration	Bond	d	E_{ads}	E_{int}
MeOH···$Al_{12}P_{12}$	A1	O···Al	1.97	−26.01	−30.76
	A2	O···Al	1.97	−25.37	−30.21
	A3	H···Al	2.64	−3.66	−3.93
		H···P	4.45		
	A4	H···Al	2.96	−3.66	−3.91
		H···P	3.35		
	A5	Al···H	2.78	−1.90	−1.97
EtOH···$Al_{12}P_{12}$	B1	O···Al	1.95	−27.23	−32.84
		H···P	3.13		
	B2	O···Al	1.97	−26.59	−32.45
		H···P	2.94		
	B3	O···Al	1.95	−27.03	−32.39
	B4	O···Al	1.95	−26.44	−32.17
		H···P	3.14		
	B5	O···Al	1.96	−26.21	−31.50
	B6	H···Al	2.69	−4.47	−4.91
		H···P	2.76		
	B7	H1···P1	2.65	−4.68	−4.84
		H2···P2	3.30		
	B8	H···Al	2.94	−2.81	−2.91
		H···P	3.20		
	B9	C···Al	3.26	−2.44	−2.52
	B10	C···Al	3.26	−2.43	−2.51

ensuring the efficacy of the $Al_{12}P_{12}$ nanocage toward adsorbing VOC molecules. The EtOH···$Al_{12}P_{12}$ complexes showed higher negative E_{ads} and E_{int} values relative to the MeOH···$Al_{12}P_{12}$ complexes. Numerically, E_{ads}/E_{int} of the interactions within the MeOH··· and EtOH···$Al_{12}P_{12}$ complexes showed values ranging from −1.90/−1.97 to −26.01/−30.76 and from −2.43/−2.51 to −27.23/−32.84 kcal mol^{-1}, respectively. It is worth noting that the selectivity of $Al_{12}P_{12}$ nanocage toward adsorbing EtOH over MeOH molecules is not guaranteed where the energy differences between MeOH··· and EtOH···$Al_{12}P_{12}$ complexes is about 2 kcal mol^{-1}.

For the sake of comparison, more favorability was denoted in the case of configurations A1 ↔ A2 and B1 ↔ B5 within the MeOH··· and EtOH···$Al_{12}P_{12}$ complexes, respectively. In the abovementioned configurations, the investigated VOCs were adsorbed on the surface of the $Al_{12}P_{12}$ nanocage *via* the interactions of their O atoms and the nanocage's Al atom. This finding was in line with the ESP results (Fig. 2) that confirmed the predominant nucleophilic character around the O atom in the VOCs. It was noticeable that the most preferred MeOH··· and EtOH···$Al_{12}P_{12}$ complexes were denoted in the case of the configurations A1 and B1, which had E_{ads} values of −26.01 and −27.23 kcal mol^{-1}, respectively.

2.3. SAPT calculations

To unveil the contributions of the physical energetic components to the inspected adsorption process, SAPT analysis was carried out for the optimized MeOH··· and EtOH···$Al_{12}P_{12}$ complexes within all plausible configurations. Fig. 3 illustrates the four main components of the total SAPT0 energy, namely induction (E_{ind}), electrostatic (E_{elst}), exchange (E_{exch}), and dispersion (E_{disp}).

Looking at Fig. 3, the E_{elst}, E_{ind}, and E_{disp} exhibited negative values, revealing their favorable role as attractive forces between the interacted species within the inspected complexes. It is worth mentioning that the E_{elst} forces were dominant within the most preferable configurations of the VOC···$Al_{12}P_{12}$ complexes. Such findings could be attributed to the interaction of the electron-rich oxygen atom in MeOH and EtOH with the electron-deficient aluminium atom in the $Al_{12}P_{12}$ nanocage. For instance, the E_{elst} values of the configurations A1 and B1 were −62.18 and −63.84 kcal mol^{-1}, respectively. For the other configurations (*i.e.*, A3 ↔ A5 and B6 ↔ B10), the E_{disp} component exhibited notable contributions to the overall attractive forces beyond the occurrence of the adsorptions process. While the E_{exch} component was found with positive values, ensuring its unfavorable contribution to the adsorption process of the VOCs onto the surface of the $Al_{12}P_{12}$ nanocage.

2.4. QTAIM and NCI analyses

QTAIM and NCI index analyses were employed to unveil an in-depth elucidation of the nature and origin of the interactions within the investigated complexes (Fig. 4). As demonstrated in Fig. 4, the occurrence of the adsorption process within the optimized MeOH··· and EtOH···$Al_{12}P_{12}$ complexes was assured

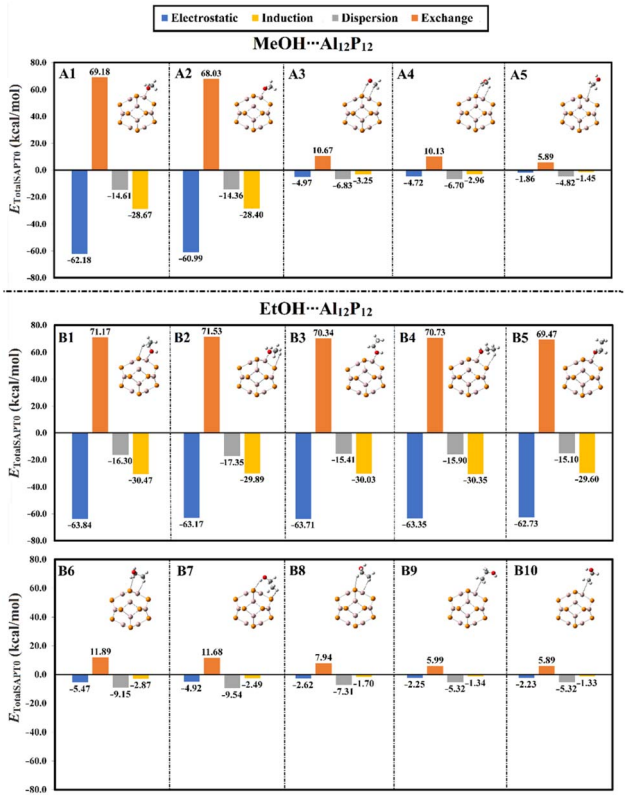

Fig. 3 Graphical representation demonstrating the energetic components of total SAPT0 energies of the optimized MeOH··· and EtOH···$Al_{12}P_{12}$ complexes within all plausible configurations.

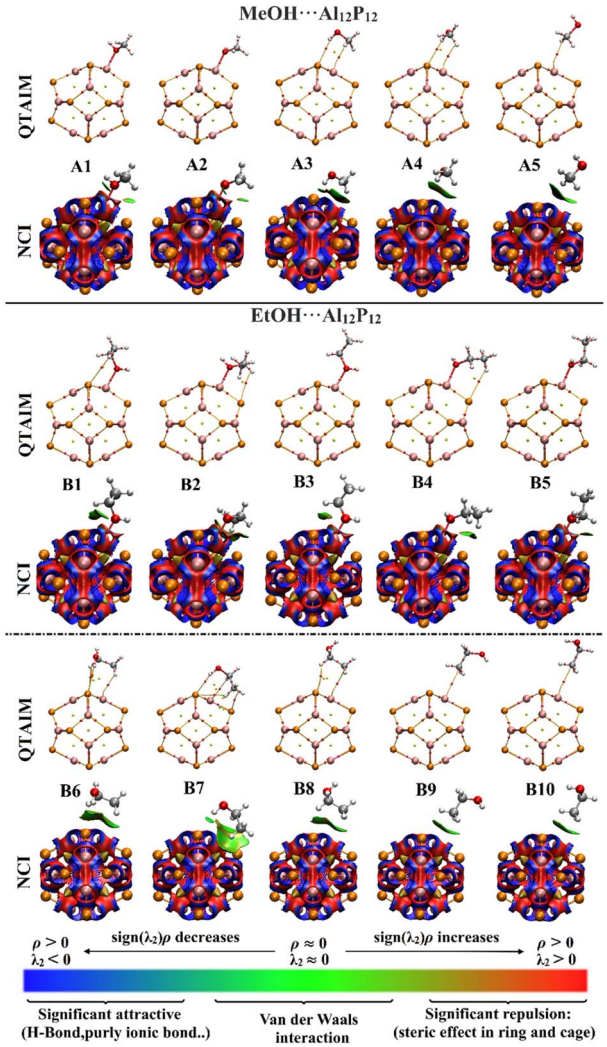

Fig. 4 QTAIM and 3D NCI plots of the optimized MeOH··· and EtOH··· $Al_{12}P_{12}$ complexes within all plausible configurations.

by the presence of bond paths (BPs) and bond critical points (BCPs) between the interacted species.

To better comprehend the interaction of VOCs with the $Al_{12}P_{12}$ nanocage, total energy density (H_b), electron density (ρ_b), Laplacian ($\nabla^2\rho_b$), kinetic electron density (G_b), local potential electron energy density (V_b), and the negative ratio of kinetic and potential electron energy density ($-G_b/V_b$) were computed at bond critical points and tabulated in Table 2. From the summarized data in Table 2, the positive $\nabla^2\rho_b$ and H_b values asserted the closed-shell nature of the interactions within the complexes under investigation. For instance, the $H_b/\nabla^2\rho_b$ values of the optimized MeOH··· and EtOH···$Al_{12}P_{12}$ complex within configuration A1 and B1 were 0.0040/0.3198 and 0.0051/0.3370 au, respectively.

Looking at 3D NCI isosurfaces displayed in Fig. 4, various types of interactions are highlighted by different colored isosurfaces; blue demonstrates a stronger hydrogen bond, green represents van der Waals interactions, and red confirms steric effects. The existence of blue-green colored isosurfaces between VOCs and the surface of the $Al_{12}P_{12}$ nanocage within the investigated complexes shed light on the propensity of the $Al_{12}P_{12}$ nanocage toward sensing the inspected VOCs.

2.5. Electronic parameters

With the incorporation of frontier molecular orbital (FMO) theory, the electronic parameters and the distribution of the molecular orbitals were outlined for the VOCs and $Al_{12}P_{12}$ before and after the adsorption process. In this regard, the energies of the highest occupied molecular orbitals (E_{HOMO}), the lowest unoccupied molecular orbitals (E_{LUMO}), Fermi level (E_{FL}), and energy gap (E_{gap}) were determined to unveil the capability of the inspected systems within monomeric and complex forms to donate and accept electrons (Table 3). Fig. 5 and 6 illustrate the distribution patterns of the molecular orbitals of the studied systems within the monomeric and complex forms, respectively.

As illustrated in Fig. 5, the HOMO and LUMO distribution patterns were observed over the electronegative and electropositive regions of the studied VOCs. Considering the $Al_{12}P_{12}$ nanocage, the P and Al atoms were generally noticed with distributions of HOMO and LUMO orbitals, respectively. Following the interactions of the adopted VOCs with $Al_{12}P_{12}$, redistribution of HOMO and LUMO orbitals was denoted, highlighting the occurrence of the adsorption process (Fig. 6). On the investigated complexes, the HOMO and LUMO levels were found over the $Al_{12}P_{12}$ nanocage.

Table 2 Topological features at BCPs of the optimized MeOH··· and EtOH···$Al_{12}P_{12}$ complexes within all the plausible configurations. All parameters are provided in au

Complexes	Configuration	Bond	ρ_b	H_b	$\nabla^2\rho_b$	G_b	V_b	$-G_b/V_b$
MeOH···$Al_{12}P_{12}$	A1	O···Al	0.0505	0.0040	0.3198	0.0759	−0.0719	1.0559
	A2	O···Al	0.0499	0.0042	0.3180	0.0753	−0.0711	1.0590
	A3	H···Al	0.0086	0.0001	0.0158	0.0040	−0.0040	1.0005
		H···P	0.0119	0.0008	0.0348	0.0079	−0.0071	1.1113
	A4	H···Al	0.0610	0.0001	0.1233	0.0037	−0.0036	1.0310
		H···P	0.0610	0.0008	0.1234	0.0078	−0.0069	1.1184
	A5	Al···H	0.0074	0.0002	0.0148	0.0035	−0.0032	1.0743
EtOH···$Al_{12}P_{12}$	B1	O···Al	0.0513	0.0051	0.3370	0.0792	−0.0741	1.0682
		H···P	0.0058	0.0010	0.0172	0.0033	−0.0024	1.4054
	B2	O···Al	0.0503	0.0039	0.3171	0.0754	−0.0716	1.0539
		H···P	0.0089	0.0013	0.0280	0.0057	−0.0043	1.3059
	B3	O···Al	0.0514	0.0047	0.3346	0.0789	−0.0742	1.0633
	B4	O···Al	0.0509	0.0051	0.3345	0.0785	−0.0734	1.0696
		H···P	0.0057	0.0009	0.0170	0.0033	−0.0024	1.4001
	B5	O···Al	0.0510	0.0045	0.3295	0.0779	−0.0733	1.0618
	B6	H···Al	0.0082	0.0002	0.0162	0.0038	−0.0036	1.0635
		H···P	0.0095	0.0010	0.0298	0.0064	−0.0054	1.1933
	B7	H1···P1	0.0115	0.0008	0.0340	0.0077	−0.0069	1.1193
		H2···P2	0.0050	0.0007	0.0144	0.0029	−0.0021	0.7427
	B8	H···Al	0.0067	0.0001	0.0137	0.0033	−0.0031	1.0446
		H···P	0.0052	0.0009	0.0153	0.0029	−0.0020	1.4400
	B9	C···Al	0.0064	0.0001	0.0137	0.0033	−0.0032	0.9681
	B10	C···Al	0.0065	0.0001	0.0138	0.0033	−0.0032	0.9684

Table 3 Computed electronic parameters (in eV) of the optimized VOCs and $Al_{12}P_{12}$ nanocage within the monomeric and complex forms

System	Configuration	E_{HOMO}	E_{FL}	E_{LUMO}	E_{gap}
MeOH		−9.577	−4.523	0.531	10.108
EtOH		−9.447	−4.472	0.502	9.949
$Al_{12}P_{12}$		−7.755	−5.389	−3.024	4.731
MeOH···$Al_{12}P_{12}$	A1	−7.430	−5.063	−2.695	4.735
	A2	−7.424	−5.054	−2.683	4.742
	A3	−7.842	−5.473	−3.104	4.737
	A4	−7.843	−5.476	−3.109	4.735
	A5	−7.766	−5.402	−3.038	4.727
EtOH···$Al_{12}P_{12}$	B1	−7.398	−5.029	−2.660	4.738
	B2	−7.400	−5.036	−2.672	4.728
	B3	−7.393	−5.024	−2.654	4.739
	B4	−7.384	−5.020	−2.656	4.729
	B5	−7.389	−5.020	−2.651	4.738
	B6	−7.836	−5.469	−3.101	4.736
	B7	−7.851	−5.484	−3.118	4.733
	B8	−7.723	−5.359	−2.994	4.729
	B9	−7.757	−5.395	−3.034	4.724
	B10	−7.757	−5.393	−3.030	4.726

Upon the listed data in Table 3, notable changes in the E_{HOMO}, E_{FL}, E_{LUMO}, and E_{gap} values following the adsorption of the VOCs on the $Al_{12}P_{12}$ nanocage were denoted, confirming the occurrence of the adsorption process. For example, the E_{HOMO} of the pure $Al_{12}P_{12}$ nanocage showed a value of −7.755 eV and changed to −7.430 and −7.398 eV after adsorbing MeOH and EtOH within the configurations A1 and B1, respectively. An apparent alteration in the E_{gap} values of the studied systems was also detected, outlining the prominent effect of the adsorption process of the MeOH and EtOH on the surface of the $Al_{12}P_{12}$ nanocage. As an illustration, the E_{gap} value of pure $Al_{12}P_{12}$ nanocage was 4.731 eV, which changed to 4.735 and 4.738 eV following the adsorption process within the configurations A1 and B1 of the MeOH··· and EtOH···$Al_{12}P_{12}$ complexes, respectively.

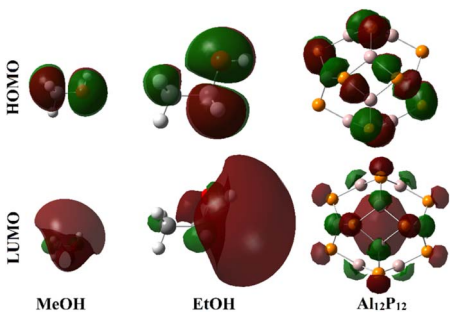

Fig. 5 Plots of the distribution patterns of HOMO and LUMO of the MeOH, EtOH, and $Al_{12}P_{12}$ monomers.

2.6. Global reactivity descriptors

In an attempt to clarify the effect of the adsorption process of the MeOH and EtOH molecules on the $Al_{12}P_{12}$ nanocage, global reactivity descriptors of the monomeric and complex forms of the studied systems were evaluated. Numerous parameters, comprising ionization potential (IP), electron affinity (EA), chemical potential (μ), global hardness (η), global softness (S), electrophilicity index (ω), and work function (Φ), were calculated and are compiled in Table 4.

Relying on the summarized data in Table 4, substantial alterations in the values of global reactivity descriptors of the

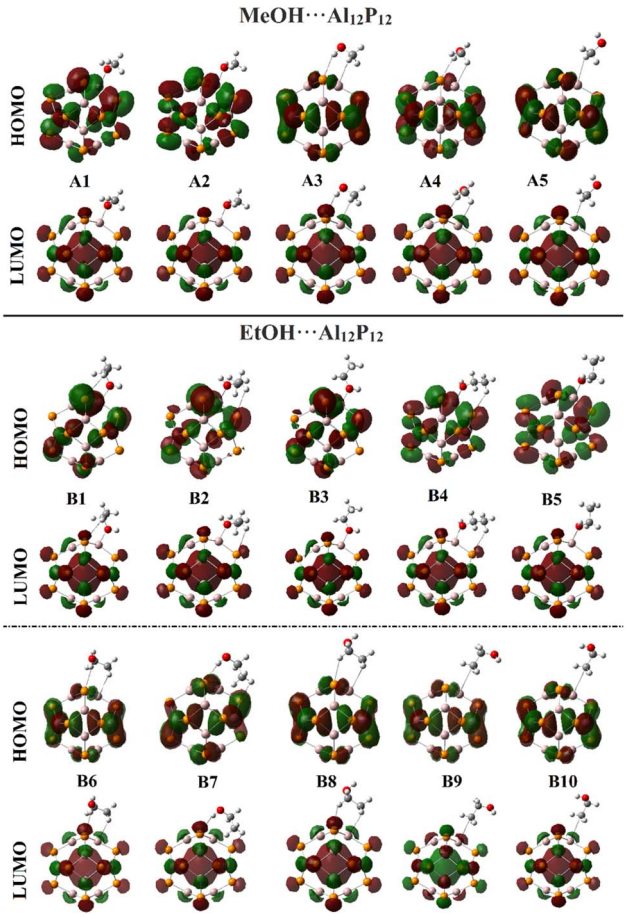

Fig. 6 Plots of the distributions patterns of HOMO and LUMO of the optimized MeOH··· and EtOH···$Al_{12}P_{12}$ complexes in all the plausible configurations.

$Al_{12}P_{12}$ before and following the adsorption process were observed, outlining the influence of the adsorption process on the reactivity character of the utilized nanocage. For instance, the IP value of pure $Al_{12}P_{12}$ nanocage was 7.755 eV and altered to 7.430 and 7.398 eV following interaction with VOCs within configurations A1 and B1, respectively. Apparently, upward and downward shifts in the η and S values were observed following the adsorption process. As numerical evidence, η of pure $Al_{12}P_{12}$ nanocage was 2.366 eV and boosted to 2.368 and 2.369 eV for the configurations A1 and B1, respectively. Remarkably, the alterations in work function affirmed the potency of $Al_{12}P_{12}$ nanocage as a promising sensing material for MeOH and EtOH molecules.

2.7. DOS analysis

DOS analysis was executed to unveil the change in the electronic characteristics of the $A_{12}P_{12}$ nanocage after the adsorption of MeOH and EtOH molecules. Fig. 7 and 8 depict the DOS plots of the $Al_{12}P_{12}$ nanocage before and following the adsorption process within all plausible configurations of the VOC···$Al_{12}P_{12}$ complexes, respectively.

Notably, new peaks were detected by comparing the DOS plots of the $Al_{12}P_{12}$ nanocage before and following the adsorption process (Fig. 7 and 8, respectively). This result outlined the

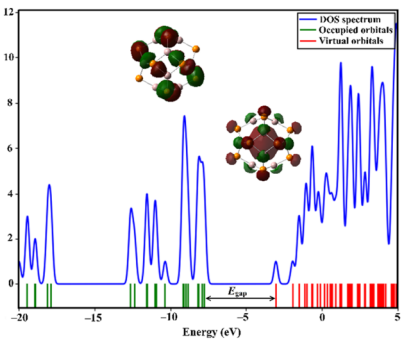

Fig. 7 The DOS plot for the pure $Al_{12}P_{12}$ nanocage before the adsorption process.

Table 4 Global indices descriptors of the monomeric and complex forms of the investigated VOCs and $Al_{12}P_{12}$ nanocage

System	Configuration	IP (eV)	EA (eV)	μ (eV)	η (eV)	S (eV^{-1})	ω (eV)	Φ (eV)
MeOH		9.577	−0.531	−4.523	5.054	0.198	2.024	4.523
EtOH		9.447	−0.502	−4.472	4.975	0.201	2.010	4.472
$Al_{12}P_{12}$		7.755	3.024	−5.389	2.366	0.423	6.139	5.389
MeOH···$Al_{12}P_{12}$	A1	7.430	2.695	−5.063	2.368	0.422	5.413	5.063
	A2	7.424	2.683	−5.054	2.371	0.422	5.386	5.054
	A3	7.842	3.104	−5.473	2.369	0.422	6.323	5.473
	A4	7.843	3.109	−5.476	2.367	0.422	6.334	5.476
	A5	7.766	3.038	−5.402	2.364	0.423	6.173	5.402
EtOH···$Al_{12}P_{12}$	B1	7.398	2.660	−5.029	2.369	0.422	5.338	5.029
	B2	7.400	2.672	−5.036	2.364	0.423	5.364	5.036
	B3	7.393	2.654	−5.024	2.370	0.422	5.326	5.024
	B4	7.384	2.656	−5.020	2.364	0.423	5.329	5.020
	B5	7.389	2.651	−5.020	2.369	0.422	5.319	5.020
	B6	7.836	3.101	−5.469	2.368	0.422	6.315	5.469
	B7	7.851	3.118	−5.484	2.367	0.423	6.355	5.484
	B8	7.723	2.994	−5.359	2.364	0.423	6.072	5.359
	B9	7.757	3.034	−5.395	2.362	0.423	6.163	5.395
	B10	7.757	3.030	−5.393	2.363	0.423	6.155	5.393

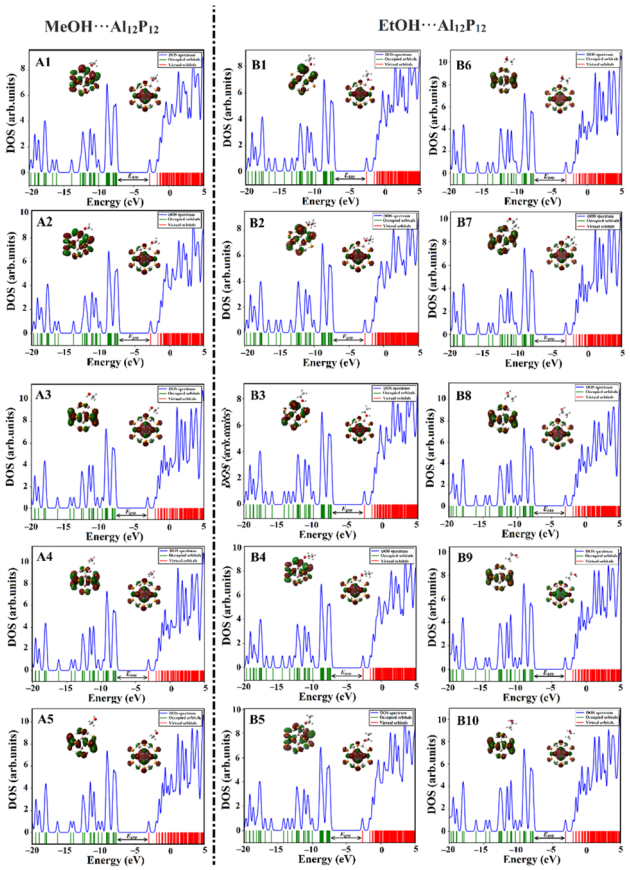

Fig. 8 The DOS plots for $Al_{12}P_{12}$ nanocage following the adsorption process of the optimized MeOH··· and EtOH···$Al_{12}P_{12}$ complexes within all plausible configurations.

influential effect of adsorbing VOCs on the electrical characteristics of the $Al_{12}P_{12}$ nanocage. For instance, additional peaks in the valence region were denoted from −13.50 to −18.00 eV in the DOS plots of almost all studied configurations. The variations in energy gap values were scrutinized for all studied complexes, confirming the ability of the studied $Al_{12}P_{12}$ nanocage to sense VOCs with disparate efficiencies.

2.8. Thermodynamic parameters

To gain a thorough understanding of the adsorption process within the MeOH··· and EtOH···$Al_{12}P_{12}$ complexes, thermodynamic parameters (*i.e.*, changes in enthalpy (ΔH), Gibbs free energy (ΔG), and entropy (ΔS)) were calculated for all the investigated complexes, and the outcomes are presented in Table 5.

According to the data listed in Table 5, the negative values of ΔG confirm the spontaneity of the adsorption process within the most preferable configurations of the VOC···$Al_{12}P_{12}$ complexes. Significantly, the exothermic nature was noticed and confirmed by negative ΔH values for the optimized VOC··· $Al_{12}P_{12}$ complexes within all inspected configurations. Remarkably, small negative ΔS values were obtained, unveiling the randomness in all studied complexes. In alignment with the E_{ads} results, configurations A1 and B1 of the VOC···$Al_{12}P_{12}$ complexes showed the highest negative values of thermodynamic energetic quantities. For instance, configuration B1 was thermodynamically stable with negative ΔG, ΔH, and ΔS values of −14.33, −25.71, and −0.038 kcal mol^{-1}, respectively. The abovementioned observations outlined the proficiency of $Al_{12}P_{12}$ nanocage toward sensing the studied VOCs.

Table 5 Thermodynamic parameters of the optimized MeOH··· and EtOH···$Al_{12}P_{12}$ complexes within all plausible configurations are in kcal mol^{-1}

Complex	Configuration	ΔG	ΔH	ΔS
MeOH···$Al_{12}P_{12}$	A1	−13.00	−24.32	−0.038
	A2	−12.75	−23.74	−0.037
	A3	6.03	−2.64	−0.029
	A4	6.00	−2.65	−0.029
	A5	5.98	−0.86	−0.023
EtOH···$Al_{12}P_{12}$	B1	−14.33	−25.71	−0.038
	B2	−13.43	−24.99	−0.039
	B3	−14.37	−25.47	−0.037
	B4	−13.99	−24.97	−0.037
	B5	−13.76	−24.64	−0.036
	B6	5.99	−3.47	−0.032
	B7	5.96	−3.69	−0.032
	B8	6.61	−1.79	−0.028
	B9	5.68	−1.32	−0.023
	B10	6.42	−1.27	−0.026

2.9. IR and Raman spectra

To ensure the occurrence of the adsorption process of the MeOH and EtOH molecules on the $Al_{12}P_{12}$ nanocage, IR and Raman spectra were extracted for pure $Al_{12}P_{12}$ nanocage (Fig. 9) and the optimized MeOH··· and EtOH···$Al_{12}P_{12}$ complexes within all plausible configurations (Fig. S1 and S2†). Fig. 10 represents plots of IR and Raman spectra of the optimized MeOH··· and EtOH···$Al_{12}P_{12}$ complexes within configurations A1 and B1 as an illustration.

As depicted in Fig. 9(a), the most noticeable IR band in pure $Al_{12}P_{12}$ nanocage was ascribed to Al···P stretching that appeared at 550 cm^{-1}. Following the adsorption of VOCs on the $Al_{12}P_{12}$ nanocage, the Al···P stretching vibrations were denoted with distinct changes in the intensities within the studied complexes (Fig. 10(a)). Obviously, new additional bands appeared in all studied complexes, affirming the substantial adsorption of MeOH and EtOH on $Al_{12}P_{12}$ nanocage (Fig. S1†).

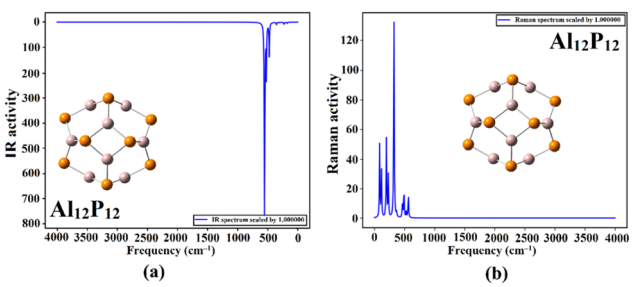

Fig. 9 Plots of (a) IR and (b) Raman spectra of pure $Al_{12}P_{12}$ nanocage.

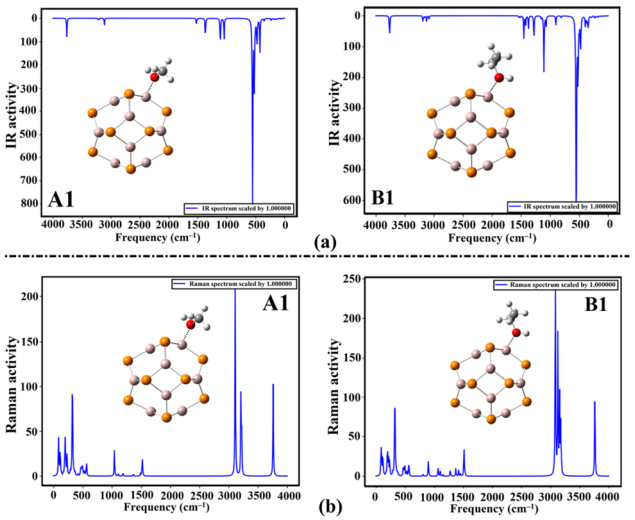

Fig. 10 Plots of (a) IR and (b) Raman spectra of the optimized MeOH⋯ and EtOH⋯$Al_{12}P_{12}$ complexes within configurations A1 and B1.

Similarly, significant alterations in the Raman spectra were noticed between the pure and complex forms of the $Al_{12}P_{12}$ nanocage (Fig. 10(b)). Overall, the notable difference in the IR and Raman spectra (Fig. S1 and S2,† respectively) announced the potential efficacy of the $Al_{12}P_{12}$ nanocage in detecting MeOH and EtOH molecules.

2.10. Recovery time

Recovery time (τ) values were computed for the optimized MeOH⋯ and EtOH⋯$Al_{12}P_{12}$ complexes within all plausible configurations toward a better comprehension of the required time for the VOC to separate from the surface of the $Al_{12}P_{12}$ nanocage (Table 6).

Relying on the recorded data in Table 6, the τ findings were directly proportional to the E_{ads} values, revealing that the time required for VOC to dissociate from the adsorbent surface increased with augmenting E_{ads} value. For the sake of clarification, the highest negative E_{ads} values were ascribed to the EtOH⋯$Al_{12}P_{12}$ complexes, which were denoted with longer τ values compared to MeOH⋯$Al_{12}P_{12}$ complexes. As numerical evidence, the configurations A1 and B1 of the MeOH⋯ and EtOH⋯$Al_{12}P_{12}$ complexes possessed the most pronounced negative E_{ads} values of −26.01 and −27.23 kcal mol^{-1} accompanied with τ values of 1.09×10^{10} and 8.54×10^{10} ms, respectively. Consequently, the $Al_{12}P_{12}$ nanocage was considered an appropriate sensor for MeOH and EtOH molecules.

Table 6 The calculated τ values of the optimized MeOH⋯ and EtOH⋯$Al_{12}P_{12}$ complexes within all plausible configurations

Complex	Configuration	τ (ms)
MeOH⋯$Al_{12}P_{12}$	A1	1.09×10^{10}
	A2	3.72×10^{9}
	A3	4.78×10^{-7}
	A4	4.78×10^{-7}
	A5	2.46×10^{-8}
EtOH⋯$Al_{12}P_{12}$	B1	8.54×10^{10}
	B2	2.91×10^{10}
	B3	6.10×10^{10}
	B4	2.26×10^{10}
	B5	1.53×10^{10}
	B6	1.87×10^{-6}
	B7	2.66×10^{-6}
	B8	1.14×10^{-7}
	B9	6.11×10^{-8}
	B10	6.01×10^{-8}

3. Computational methods

The adsorption amplitude of VOCs (*i.e.*, MeOH and EtOH) over the $Al_{12}P_{12}$ nanocage was fully investigated using a plethora of DFT computations with the aid of the Gaussian 09 package.[43] For the investigated systems, the geometrical optimization accompanied by frequency computations was carried out at the M06-2X[44] method simultaneously with a 6-31+G* basis set.

To illustrate the nucleophilic and electrophilic characters of the MeOH, EtOH, and $Al_{12}P_{12}$, the electrostatic potential (ESP) analysis was conducted. Using an electron density envelope of 0.002 au,[45] surface electrostatic potential extrema ($V_{s,min}/V_{s,max}$) and molecular electrostatic potential (MEP) maps were evaluated and extracted to provide numerical and graphical explanations for the investigated systems, respectively. The $V_{s,min}/V_{s,max}$ were obtained by adopting the Multiwfn 3.7 software.[46]

The efficacy of $Al_{12}P_{12}$ nanocage toward adsorbing VOCs was thoroughly determined in terms of adsorption (E_{ads}) and interaction (E_{int}) energies. For the VOC⋯$Al_{12}P_{12}$ complexes, E_{ads} and E_{int} were computed utilizing the counterpoise corrected (CC) method to eliminate the basis set superposition error (BSSE),[47] relying on eqn (1) and (2), respectively.

$$E_{ads} = E_{VOC\cdots Al12P12} - (E_{VOC} + E_{Al_{12}P_{12}}) + E_{BSSE} \quad (1)$$

$$E_{int} = E_{VOC\cdots Al_{12}P_{12}} - (E_{VOC\ in\ complex} + E_{Al_{12}P_{12}\ in\ complex}) + E_{BSSE} \quad (2)$$

where $E_{VOC\cdots Al_{12}P_{12}}$, E_{VOC}, and $E_{Al_{12}P_{12}}$ represent the energies of investigated complexes, isolated VOCs, and $Al_{12}P_{12}$ nanocage, respectively. Whereas the $E_{VOC\ in\ complex}$ and $E_{Al_{12}P_{12}\ in\ complex}$ identify the energies of the MeOH/EtOH molecules and $Al_{12}P_{12}$ nanocage based on their coordinates in the complex form.

Moreover, SAPT analysis was performed employing the SAPT0 level of truncation using the PSI4 code.[48] In the context of SAPT, the total energy (E^{SAPT0}) was divided into E_{ind}, E_{elst}, E_{exch}, and E_{disp}. E^{SAPT0} was evaluated utilizing eqn (3).[49–51]

$$E^{SAPT0} = E_{elst} + E_{exch} + E_{ind} + E_{disp} \quad (3)$$

Wavefunction analyses, including NCI index and QTAIM, were executed for the VOC⋯$Al_{12}P_{12}$ complexes using the Multiwfn 3.7 software[46] and visualized by the Visual Molecular Dynamics program.[52] With the inclusion of QTAIM, the BPs and BCPs between the interacted species were extracted. The topological parameters were evaluated for all the studied complexes. Considering the NCI index, the 3D colored isosurfaces were

extracted depending on the sign(λ_2)ρ varying between blue (−0.035 au) to red (0.020 au).

Toward obtaining an adequate illustration of the electronic properties before and following the adsorption process, the FMO theory was implemented. In this regard, the HOMO/LUMO distribution patterns were plotted for the monomeric and complex forms. Similarly, HOMO/LUMO energies (E_{HOMO}/E_{LUMO}) were determined. Upon the obtained E_{HOMO} and E_{LUMO} values, the E_{gap} and E_{FL} values were determined as follows:

$$E_{FL} = E_{HOMO} + \frac{E_{LUMO} - E_{HOMO}}{2} \quad (4)$$

$$E_{gap} = E_{LUMO} - E_{HOMO} \quad (5)$$

Based on the data obtained from FMO, the IP and EA were predestined based on eqn (6) and (7).

$$IP \approx -E_{HOMO} \quad (6)$$

$$EA \approx -E_{LUMO} \quad (7)$$

By applying Koopman's theorem,[53] the chemical reactivity descriptors of molecules could be predicted based on quantum mechanical descriptors. Accordingly, η, ω, S, and μ were calculated utilizing eqn (8)–(11).

$$\eta = \frac{E_{LUMO} - E_{HOMO}}{2} \quad (8)$$

$$\mu = \frac{E_{LUMO} + E_{HOMO}}{2} \quad (9)$$

$$s = \frac{1}{\eta} \quad (10)$$

$$\omega = \frac{\mu^2}{2\eta} \quad (11)$$

Afterwards, the Φ was calculated to determine the sensing ability of the studied nanocages using eqn (12),[54] where $V_{el(+\infty)}$ identifies the electrostatic potential far from the nanocage surface that was postulated to be ≈0.

$$\Phi = V_{el(+\infty)} - E_{FL} \quad (12)$$

To elucidate the influence of the adsorption process on the electronic properties of the utilized nanocage, density of states (DOS) plots were extracted within an energy range of −20 to +5 eV before and following the adsorption process based on eqn (13) employing the GaussSum software.[55]

$$TDOS(E) = \sum_i \delta(E - \varepsilon_i) \quad (13)$$

where ε and δ represent the eigenvalue set of single-particle Hamilton and Dirac delta function, respectively.

To assess the thermodynamic parameters of the inspected complexes, ΔH, ΔG, and ΔS were evaluated based on frequency calculations as follows:

$$\Delta M = M_{VOC\cdots Al_{12}P_{12}} - (M_{VOC} + M_{Al_{12}P_{12}}) + E_{BSSE} \quad (14)$$

$$\Delta S = -(\Delta G - \Delta H)/T \quad (15)$$

whereas M indicates the quantity of G and H. The M of investigated complexes, VOCs, and nanocage were represented by $M_{VOC\cdots Al_{12}P_{12}}$, M_{VOC}, and $M_{Al_{12}P_{12}}$, respectively. T refers to temperature with a value of 298.15 K. Upon frequency computations, plots of IR and Raman spectra were extracted with the aid of GaussSum software.[55] Recovery time (τ) was subsequently calculated to evaluate the feasibility of the desorption process within the complexes understudy using formula (16),[56,57] where ν_0 and K represent the attempt frequency with a value of 10^{12} s^{-1} and Boltzmann's constant, respectively.

$$\tau = \nu_0^{-1} \exp(-\Delta E_{ads}/KT) \quad (16)$$

4. Conclusions

The sensitivity of $Al_{12}P_{12}$ nanocage toward sensing MeOH and EtOH molecules was investigated in all plausible configurations utilizing numerous DFT calculations. The ESP outcomes unveiled the existence of evident nucleophilic and electrophilic regions over the surface of the MeOH and EtOH molecules, in particular around the O and C/H atoms, respectively. In comparison, the $Al_{12}P_{12}$ nanocage was observed with nucleophilic and electrophilic regions surrounding P and Al atoms, respectively. According to the energetic findings, the adsorption process showed higher preferability in the case of the EtOH$\cdots$$Al_{12}P_{12}$ complexes compared to the MeOH$\cdots$$Al_{12}P_{12}$ complexes with E_{int}/E_{ads} values up to −32.84/−27.23 and −30.76/−26.01 kcal mol^{-1}, respectively. SAPT affirmations revealed the E_{elst} forces with immense contributions to the attractive forces within the most preferable configurations of the VOC$\cdots$$Al_{12}P_{12}$ complexes. QTAIM and NCI index results assured the noncovalent nature of the interaction within the studied complexes. The noticeable changes in molecular orbitals distribution patterns of MeOH/EtOH/$Al_{12}P_{12}$ nanocage, the electronic parameters, and the global reactivity descriptors highlighted the occurrence of the adsorption of VOCs on $Al_{12}P_{12}$ nanocage. Remarkably, thermodynamic parameters substantiated the exothermic character of the VOC$\cdots$$Al_{12}P_{12}$ complexes within all plausible configurations. Thermodynamic parameters were denoted with negative values, demonstrating the spontaneous exothermic nature of the most investigated complexes. The appearance of new peaks in DOS plots confirmed the occurrence of the adsorption process between the studied VOCs and $Al_{12}P_{12}$ nanocage. Based on IR and Raman spectra findings, the occurrence of the adsorption process was ensured by the appearance of new bands in IR and Raman spectra. Recovery time results addressed the $Al_{12}P_{12}$ nanocage as an appropriate sensor for MeOH and EtOH molecules with τ values ranging from 6.11×10^{-8} to 8.54×10^{10} ms. The emerging findings would provide a comprehensive insight into the efficiency of the $Al_{12}P_{12}$ nanocage in detecting VOCs, especially for MeOH and EtOH molecules.

Author contributions

Conceptualization, Mahmoud A. A. Ibrahim and Tamer Shoeib; methodology, Mahmoud A. A. Ibrahim, Nayra A. M. Moussa, and Ahmed M. Awad; software, Mahmoud A. A. Ibrahim; formal analysis, Manar H. A. Hamad; investigation, Manar H. A. Hamad and Nayra A. M. Moussa; resources, Mahmoud A. A. Ibrahim, Shaban R. M. Sayed, Omar H. Abd-Elkader and Tamer Shoeib; data curation, Manar H. A. Hamad; writing—original draft preparation, Manar H. A. Hamad; writing—review and editing, Mahmoud A. A. Ibrahim, Nayra A. M. Moussa, Shaban R. M. Sayed, Omar H. Abd-Elkader, Muhammad Naeem Ahmed, Ahmed M. Awad, and Tamer Shoeib; visualization, Manar H. A. Hamad and Muhammad Naeem Ahmed; supervision, Mahmoud A. A. Ibrahim; project administration, Mahmoud A. A. Ibrahim, Nayra A. M. Moussa and Tamer Shoeib. All authors have read and agreed to the published version of the manuscript.

Conflicts of interest

There are no conflicts to declare.

Acknowledgements

The authors are grateful to the Researchers Supporting Project number (RSP2024R468), King Saud University, Riyadh, Saudi Arabia. The computational work was completed with resources provided by the CompChem Lab (Minia University, Egypt, **http://hpc.compchem.net/**), Center for High-Performance Computing (Cape Town, South Africa, **http://www.chpc.ac.za**), and Bibliotheca Alexandrina (**http://hpc.bibalex.org**).

References

1 S. Haghgoo and A. R. Nekoei, *RSC Adv.*, 2021, **11**, 17377–17390.
2 M. Yoosefian, M. Zahedi, A. Mola and S. Naserian, *Appl. Surf. Sci.*, 2015, **349**, 864–869.
3 A. Kose, N. Yuksel and M. F. Fellah, *Diamond Relat. Mater.*, 2022, **124**, 108921.
4 S. Sajjad, M. A. Hashmi, T. Mahmood and K. Ayub, *J. Mol. Graphics Modell.*, 2020, **101**, 107748.
5 A. L. P. Silva, A. C. A. Silva, C. N. Navis and J. de Jesus Gomes Varela Júnior, *J. Nanopart. Res.*, 2021, **23**, 108.
6 A. Allangawi, M. A. Gilani, K. Ayub and T. Mahmood, *Int. J. Hydrogen Energy*, 2023, **48**, 16663–16677.
7 J. Beheshtian, Z. Bagheri, M. Kamfiroozi and A. Ahmadi, *J. Mol. Model.*, 2012, **18**, 2653–2658.
8 F. Ullah, N. Kosar, A. Ali, Maria, T. Mahmood and K. Ayub, *Phys. E*, 2020, **118**, 113906.
9 F. Ullah, S. Irshad, S. Khan, M. A. Hashmi, R. Ludwig, T. Mahmood and K. Ayub, *J. Phys. Chem. Solids*, 2021, **151**, 109914.
10 F. Ullah, N. Kosar, K. Ayub, M. A. Gilani and T. Mahmood, *New J. Chem.*, 2019, **43**, 5727–5736.
11 R. Padash, M. R. Esfahani and A. S. Rad, *J. Biomol. Struct. Dyn.*, 2021, **39**, 5427–5437.
12 A. S. M. Rady, N. A. M. Moussa, L. A. Mohamed, P. A. Sidhom, S. R. M. Sayed, M. K. Abd El-Rahman, E. Dabbish, T. Shoeib and M. A. A. Ibrahim, *Heliyon*, 2023, **9**, e18690.
13 F. Younas, M. Y. Mehboob, K. Ayub, R. Hussain, A. Umar, M. U. Khan, Z. Irshad and M. Adnan, *J. Comput. Biophys. Chem.*, 2020, **20**, 85–97.
14 S. Hussain, S. A. Shahid Chatha, A. I. Hussain, R. Hussain, M. Y. Mehboob, T. Gulzar, A. Mansha, N. Shahzad and K. Ayub, *ACS Omega*, 2020, **5**, 15547–15556.
15 H. Farrokhpour, H. Jouypazadeh and S. Vakili Sohroforouzani, *Mol. Phys.*, 2020, **118**, 1626506.
16 R. Padash, M. Rahimi-Nasrabadi, A. Shokuhi Rad, A. Sobhani-Nasab, T. Jesionowski and H. Ehrlich, *J. Cluster Sci.*, 2018, **30**, 203–218.
17 N. Thongsai, N. Tanawannapong, J. Praneerad, S. Kladsomboon, P. Jaiyong and P. Paoprasert, *Colloids Surf., A*, 2019, **560**, 278–287.
18 S. M. Aghaei, A. Aasi, S. Farhangdoust and B. Panchapakesan, *Appl. Surf. Sci.*, 2021, **536**, 147756.
19 Y. J. Huang, D. R. Ma, J. Cao, Z. Y. Tang, L. L. Hu, Y. X. Zhang, H. N. Zhao, D. H. Xia, C. He and P. K. Wong, *Appl. Catal.*, 2023, **652**, 119031.
20 R. Si, Y. Li, J. Tian, C. Tan, S. Chen, M. Lei, F. Xie, X. Guo and S. Zhang, *Nanomater.*, 2023, **13**, 908.
21 D. Li, X. Li, J. Wang, T. Wang and Y. Wen, *Theor. Chem. Acc.*, 2023, **142**, 112.
22 S. Kaviani, I. I. Piyanzina, O. V. Nedopekin and D. A. Tayurskii, *Mater. Today Commun.*, 2022, **33**, 104851.
23 C. Wen, T. Y. Liu, D. P. Wang, Y. Q. Wang, H. P. Chen, G. Q. Luo, Z. J. Zhou, C. K. Li and M. H. Xu, *Prog. Energy Combust. Sci.*, 2023, **99**, 101098.
24 R. Koppmann, in *Hydrocarbons, Oils and Lipids: Diversity, Origin, Chemistry and Fate*, ed. H. Wilkes, Springer International Publishing, Cham, 2020, ch. 24, pp. 811–822, DOI: **10.1007/978-3-319-90569-3_24**.
25 C. Pang, R. Han, Y. Su, Y. Zheng, M. Peng and Q. Liu, *Chem. Eng. J.*, 2023, **454**, 140125.
26 X. Zhang, B. Gao, A. E. Creamer, C. Cao and Y. Li, *J. Hazard. Mater.*, 2017, **338**, 102–123.
27 F. I. Khan and A. K. Ghoshal, *J. Loss Prev. Process Ind.*, 2000, **13**, 527–545.
28 M. Weng, L. Zhu, K. Yang and S. Chen, *Environ. Monit. Assess.*, 2010, **163**, 573–581.
29 J. Li, S. Deng, G. Li, Z. Lu, H. Song, J. Gao, Z. Sun and K. Xu, *Environ. Res.*, 2022, **203**, 111821.
30 Z. Zhong, Q. Sha, J. Zheng, Z. Yuan, Z. Gao, J. Ou, Z. Zheng, C. Li and Z. Huang, *Sci. Total Environ.*, 2017, **583**, 19–28.
31 Y. Wang, C. Wang, K. Zeng, S. Wang, H. Zhang, X. Li, Z. Wang and C. Zhang, *Appl. Surf. Sci.*, 2022, **576**, 151797.
32 Y. Huang, S. S. Ho, Y. Lu, R. Niu, L. Xu, J. Cao and S. Lee, *Molecules*, 2016, **21**, 56.
33 J. Wang, Y. Zhang, Z. Wu, S. Luo, W. Song and X. Wang, *J. Environ. Sci.*, 2022, **114**, 322–333.

34 L. Zhu, D. Shen and K. H. Luo, *J. Hazard. Mater.*, 2020, **389**, 122102.
35 Q. Zhao, Z. Zhao, R. Rao, Y. Yang, S. Ling, F. Bi, X. Shi, J. Xu, G. Lu and X. Zhang, *J. Colloid Interface Sci.*, 2022, **627**, 385–397.
36 B. Guieysse, C. Hort, V. Platel, R. Munoz, M. Ondarts and S. Revah, *Biotechnol. Adv.*, 2008, **26**, 398–410.
37 C. Zhang, X. Gao, J. Qin, Q. Guo, H. Zhou and W. Jin, *J. Hazard. Mater.*, 2021, **402**, 123817.
38 R. A. Alsaigh, S. Rahman, F. S. Alfaifi, M. A. Al-Gawati, R. Shallaa, F. Alzaid, A. F. Alanazi, H. Albrithen, K. E. Alzahrani, A. K. Assaifan, A. N. Alodhayb and P. E. Georghiou, *Chemosensors*, 2022, **10**, 452.
39 V. Nagarajan and R. Chandiramouli, *J. Mol. Graphics Modell.*, 2018, **81**, 97–105.
40 A. M. Tolmachev, D. A. Firsov, T. A. Kuznetsova and K. M. Anuchin, *Prot. Met. Phys. Chem. Surf.*, 2009, **45**, 163–168.
41 P. K. Adak, S. K. Singh, J. Singh, S. Mahesh, M. K. Jain, P. A. K. Sagar, S. Banerjee and M. A. S. Khan, *J. Mol. Model.*, 2022, **28**, 400.
42 F. Khaliq, K. Ayub, T. Mahmood, S. Muhammad, S. Tabassum and M. A. Gilani, *Mater. Sci. Semicond. Process.*, 2021, **135**, 106122.
43 M. J. Frisch, G. W. Trucks, H. B. Schlegel, G. E. Scuseria, M. A. Robb, J. R. Cheeseman, G. Scalmani, V. Barone, B. Mennucci, G. A. Petersson, H. Nakatsuji, M. Caricato, X. Li, H. P. Hratchian, A. F. Izmaylov, J. Bloino, G. Zheng, J. L. Sonnenberg, M. Hada, M. Ehara, K. Toyota, R. Fukuda, J. Hasegawa, M. Ishida, T. Nakajima, Y. Honda, O. Kitao, H. Nakai, T. Vreven, J. A. Montgomery, J. E. Peralta, F. Ogliaro, M. Bearpark, J. J. Heyd, E. Brothers, K. N. Kudin, V. N. Staroverov, R. Kobayashi, J. Normand, K. Raghavachari, A. Rendell, J. C. Burant, S. S. Iyengar, J. Tomasi, M. Cossi, N. Rega, J. M. Millam, M. Klene, J. E. Knox, J. B. Cross, V. Bakken, C. Adamo, J. Jaramillo, R. Gomperts, R. E. Stratmann, O. Yazyev, A. J. Austin, R. Cammi, C. Pomelli, J. W. Ochterski, R. L. Martin, K. Morokuma, V. G. Zakrzewski, G. A. Voth, P. Salvador, J. J. Dannenberg, S. Dapprich, A. D. Daniels, Ö. Farkas, J. B. Foresman, J. V. Ortiz, J. Cioslowski and D. J. Fox, *Gaussian 09 Revision E01*, Gaussian Inc., Wallingford CT, USA.
44 Y. Zhao and D. G. Truhlar, *J. Chem. Theory Comput.*, 2008, **4**, 1849–1868.
45 M. A. A. Ibrahim, *J. Mol. Model.*, 2012, **18**, 4625–4638.
46 T. Lu and F. Chen, *J. Comput. Chem.*, 2012, **33**, 580–592.
47 S. F. Boys and F. Bernardi, *Mol. Phys.*, 1970, **19**, 553–566.
48 R. M. Parrish, L. A. Burns, D. G. A. Smith, A. C. Simmonett, A. E. DePrince 3rd, E. G. Hohenstein, U. Bozkaya, A. Y. Sokolov, R. Di Remigio, R. M. Richard, J. F. Gonthier, A. M. James, H. R. McAlexander, A. Kumar, M. Saitow, X. Wang, B. P. Pritchard, P. Verma, H. F. Schaefer 3rd, K. Patkowski, R. A. King, E. F. Valeev, F. A. Evangelista, J. M. Turney, T. D. Crawford and C. D. Sherrill, *J. Chem. Theory Comput.*, 2017, **13**, 3185–3197.
49 T. M. Parker, L. A. Burns, R. M. Parrish, A. G. Ryno and C. D. Sherrill, *J. Chem. Phys.*, 2014, **140**, 094106.
50 E. G. Hohenstein and C. D. Sherrill, *J. Chem. Phys.*, 2010, **132**, 184111–184120.
51 E. G. Hohenstein, R. M. Parrish, C. D. Sherrill, J. M. Turney and H. F. Schaefer 3rd, *J. Chem. Phys.*, 2011, **135**, 174107–174119.
52 W. Humphrey, A. Dalke and K. Schulten, *J. Mol. Graphics*, 1996, **14**, 33–38.
53 M. Ernzerhof, *J. Chem. Theory Comput.*, 2009, **5**, 793–797.
54 M. R. Hossain, M. M. Hasan, M. Nishat, N.-E. Ashrafi, F. Ahmed, T. Ferdous and M. Abul Hossain, *J. Mol. Liq.*, 2021, **323**, 114627.
55 N. M. O'Boyle, A. L. Tenderholt and K. M. Langner, *J. Comput. Chem.*, 2008, **29**, 839–845.
56 H. M. Badran, K. M. Eid and H. Y. Ammar, *Results Phys.*, 2021, **23**, 103964.
57 S. Demir and M. F. Fellah, *Appl. Surf. Sci.*, 2020, **504**, 144141.